ChemComm

Formation of a core-shell droplet in a thermo-responsive ionic liquid/water mixture by optical tweezers

Journal:	*ChemComm*
Manuscript ID	CC-COM-05-2022-002699.R2
Article Type:	Communication

COMMUNICATION

Formation of a core-shell droplet in a thermo-responsive ionic liquid/water mixture by optical tweezers

Maho Tanaka,[a] Yasuyuki Tsuboi [a] and Ken-ichi Yuyama *[a]

Received 00th January 20xx,
Accepted 00th January 20xx

DOI: 10.1039/x0xx00000x

Many chemical and biological processes involve phase separation; however, controlling this is challenging. Here, we demonstrate local phase separation using optical tweezers in a thermo-responsive ionic liquid/water solution. Upon the near-infrared laser irradiation, a single droplet is formed at the focal spot. The droplet has a core consisting of highly concentrated ionic liquid. The mechanism of the core-shell droplet formation is discussed in view of the spatial distribution of optical and thermal potentials.

Phase separation in molecular solutions is associated to various chemical and biological phenomena. Solid-liquid phase separation (crystallization) is a key process for the purification and separation of solutes from a solution as well as for the preparation of crystals in X-ray crystallographic analysis.[1,2] Liquid-liquid phase separation is known to play a critical role in a variety of cellular processes, including the formation of classical membraneless organelles and other supramolecular assemblies.[3,4] Phase separation occurs spontaneously in a metastable solution through fluctuations in concentration. Chemical or physical stimuli, such as heating or cooling the solution, the application of pressure, or mixing with additives, are used to prepare metastable conditions, triggering phase separation.[5,6,7] In addition to these ways, recent advances in microfluidic devices enable selection of nucleation-growth pathways, and precise control the formation of metastable crystals is realized.[8,9,10] However, with these approaches, the separation proceeds at random in the solution, and it is difficult to predict when and where it will start.

Optical tweezers provide us with a powerful technique to control phase separation in a spatial and temporal manner. A laser beam exerts an optical force in the solute.[11] If the polarizability (α_{pol}) of the solute is larger than that of the surrounding medium (solvent molecules), a gradient force acts as an attractive force toward the focal spot. The magnitude of the force is proportional to gradient of the light intensity, so that the force weakens with distance from the focal spot. That is, the laser generates an optical potential well, U_{opt} (equation 1);

$$U_{\mathrm{opt}} = -\frac{1}{2}\alpha_{\mathrm{pol}}\boldsymbol{E}^2 \quad (1),$$

where $\boldsymbol{E}$ is the electric field vector of the incident light.[12] This optical potential plays a role in increasing the local concentration by confining the solute or in decreasing the energy barrier toward another stable state.[13,14,15,16] As a result, phase separation is triggered at the focal spot.

Wynne et al. demonstrated laser-induced phase separation and nucleation of droplets in a nitrobenzene/decane mixture.[17] They explained the mechanism by showing theoretical results on the change in the free-energy landscape under laser irradiation. Sugiyama and Masuhara et al. succeeded in inducing the crystallization of amino acids by confining their pre-nucleation clusters in the optical potential well of a continuous-wave laser beam.[18,19] Crystallization is generated even in an unsaturated solution where no spontaneous crystallization occurs.[20,21] Alexander et al. controlled the crystallization of potassium chloride by applying the optical potential well of nanosecond laser pulses.[22]

Another interesting system is a solution that shows LCST (lower critical solution temperature)-type phase separation, such as aqueous solutions of thermo-responsive polymers or alcohol/water mixtures.[23,24,25,26,27] Optical tweezers with a 1064 nm-laser beam lead to the generation of an optical potential well and a photothermal effect. The latter initiates phase separation around the focus, and the resultant condensates are attracted to U_{opt} and merge. As a result, a single liquid droplet is formed and trapped. So far, the formation of a homogeneous droplet and a coacervate droplet has been reported.[23,24,25,26,27]

In the present study, the formation of a core-shell type droplet is demonstrated by applying optical tweezers to an ionic liquid (IL)/water mixture that exhibits LCST-type phase separation (Fig. 1a). The inner core is highly concentrated IL,

[a] Department of Chemistry, Graduate School of Science, Osaka Metropolitan University, 3-3-138 Sugimoto Sumiyoshi-ku, Osaka-shi, 558-8585, Japan. E-mail: k-yuyama@omu.ac.jp

† Electronic Supplementary Information (ESI) available.
See DOI: 10.1039/x0xx00000x

while the shell is an IL-rich aqueous solution. The droplet formation dynamics are discussed from the viewpoints of the optical and thermal potentials and their spatial distributions.

The ionic liquid used is tetrabutylphosphonium 2,4-dimethylbenzenesulfonate ($[P4444]^+[2,4\text{-}MeSO_3]^-$) (Fig. 1b).[28,29] The phase diagram of the IL/water mixture is shown in Figure 1c. The experiments using optical tweezers were carried out on a mixture in which the mass fraction of the IL was 0.094. This solution separates into two phases above 49°C, and micrometer-size IL rich droplets are formed (Fig. 1d). The details of the experimental procedure are summarized in ESI (S1 & S2).

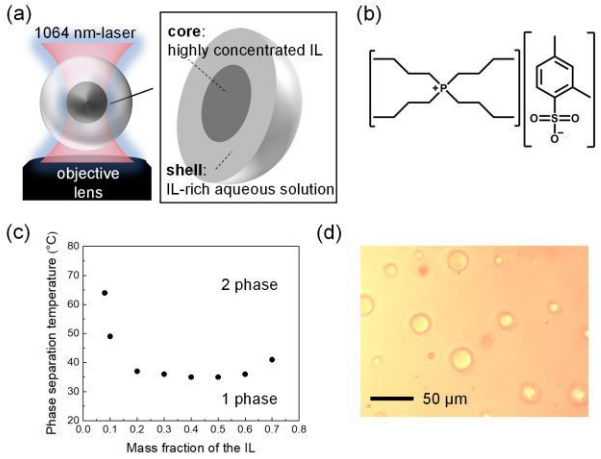

Fig. 1 (a) Schematic illustration of a core-shell type droplet formed by optical tweezers. (b) Molecular structure of the IL. (c) Phase diagram of the IL/water mixture. (d) An optical transmission image of the sample solution captured at the phase separation temperature.

Single droplet formation was clearly observed by optical transmission imaging during irradiation of a 1064 nm-laser beam, while an inner core was found after switching off the laser. The solution was uniformly heated to 36°C with a thermal plate, and the power of the laser after passing through the objective lens was tuned at 630 mW. Figure 2a shows the time evolution of micrographs around the focal spot. The solution was initially homogeneous, and nothing was seen in the micrograph [Fig. 2a (i)]. At 60 sec, a small liquid droplet with a diameter of 2.3 μm was formed [Fig. 2a (ii)]. The droplet increased in volume while being stably trapped [Fig. 2a (iii)], and the diameter of the droplet reached 8.3 μm at 420 sec [Fig. 2a (iv)]. Incidentally, the droplet keeps growing under the laser irradiation at 630 mW. The grown large droplet is released to the surrounding solution, and a new droplet starts to grow at the focal spot (S3). When the laser power is decreased, the growth is stopped. The droplet shrinks until equilibrium is reached. The size of the final microdroplet depends on the input laser power (S4).

The resultant liquid droplet started dissolving after switching off the laser (Fig. 2b). The droplet migrated randomly in the solution as it decreased in size [Fig. 2b (ii)]. Sometimes the droplet locates below or above the focal plane, causing the droplet to appear very bright [Fig. 2b (iii)]. What is important here is that the droplet did not dissolve completely (video 1). A small droplet remained and showed random motion [Fig. 2b (iv)]. This result indicates that the droplet of Fig. 2b (i) has a core-shell structure. The core-shell droplet formation can be induced with good reproducibility. Always the core remains after switching off the laser. However, the time when the droplet formation starts varies among the experiments. This is due to stochastic nature of the nucleation process.

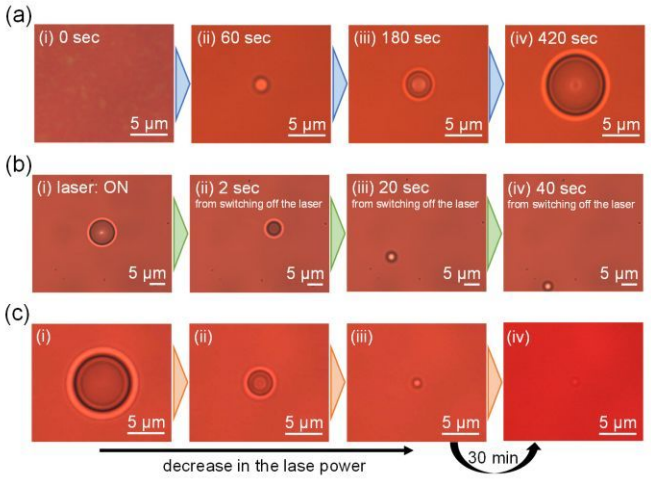

Fig. 2 Optical transmission micrographs around the focal spot (a) during laser irradiation, (b) after switching off the laser, and (c) in the process of decreasing the laser power.

It was possible to trap only the core at very low laser power intensity. Figure 2c shows optical transmission micrographs with decreasing laser power down to 20 mW. In the initial stage of decreasing the power, the droplet has a diameter of 8.0 μm [Fig. 2c (i)]. Subsequently, it shrank to a smaller size [Fig. 2c (ii)], and only the core remains at the focus at 20 mW [Fig. 2c (iii)]. The core can clearly be observed even after 30 min, although it has shrunk slightly [Fig. 2c (iv)]. Thus, the core has high stability with long lifetime exceeding 30 min (S5).

The IL concentration of the shell and core parts of the droplet was estimated by confocal Raman microspectroscopy. A calibration curve was prepared by measuring Raman spectra of IL/water mixtures with different concentrations of IL in the steady state. Figure 3a shows examples of measured spectra. Two distinct Raman bands can be observed in the C-H (2800–3000 cm^{-1}) and O-H (3000–3800 cm^{-1}) stretching regions, which are ascribed to the IL and water, respectively. The calibration curve was obtained by plotting the Raman band area ratio ($A_{2800–3000\ cm^{-1}}/A_{3000–3800\ cm^{-1}}$) against the mass fraction of the IL (the inset in Fig. 3a).

In the case of the shell, we prepared a droplet with a diameter of 8 μm and measured a spatially resolved spectrum at a point 4 μm away from the focus of the 1064 nm-laser. On the other hand, the core was trapped by decreasing the laser power in a similar way to that for the approach shown in Fig. 2c. Then, the spectrum at the laser focus was measured. The shell showed an increased signal in the C-H stretching region (Fig. 3b). In the core, the scattering intensity in the same region was a bit higher than that of the shell (Fig. 3b). The mass fraction of the shell and the core were estimated to be 0.45 and 0.48,

respectively. These values might be underestimated because the detection area of the Raman spectroscopy is 1.5 μm in diameter. In both measurements, the signal from the surrounding solution might be involved.

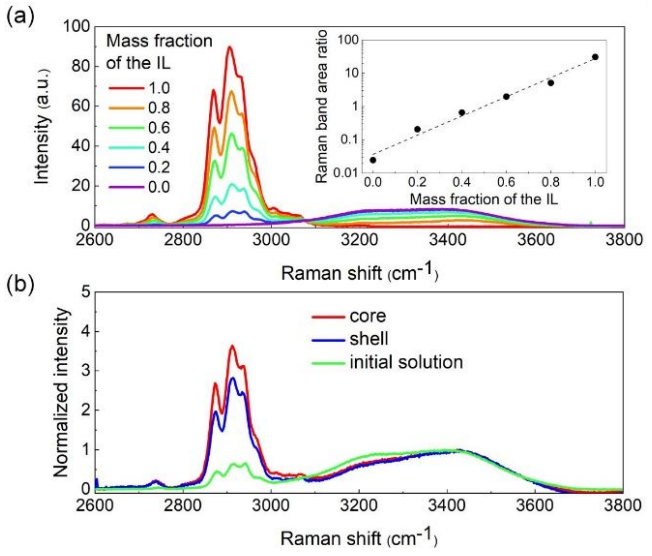

Fig. 3 (a) Raman spectra of IL/mixtures with different concentrations. The inset is the Raman band area ratio against the mass fraction of the IL. (b) Raman spectra of the shell, and the core, and the initial solution. The spectra are normalized at the respective peaks in the O-H stretching region.

For further characterization, we used a fluorescence probe: we added a solvatochromic fluorescent dye (coumarin 153) of 1.3 μM to observe the droplet by fluorescence imaging. Coumarin 153 is known to exhibit an intramolecular charge-transfer band whose peak position is sensitive to the polarity of the surrounding medium.[30] With a decrease in the polarity of the surrounding medium, the emission maximum shifts toward a shorter wavelength. Figures 4a and 4b show fluorescence images and spectra of the shell and core, respectively. The shell showed yellow fluorescence, while the core was green. The respective peaks of the fluorescence spectra were observed at 543.0 and 534.7 nm.

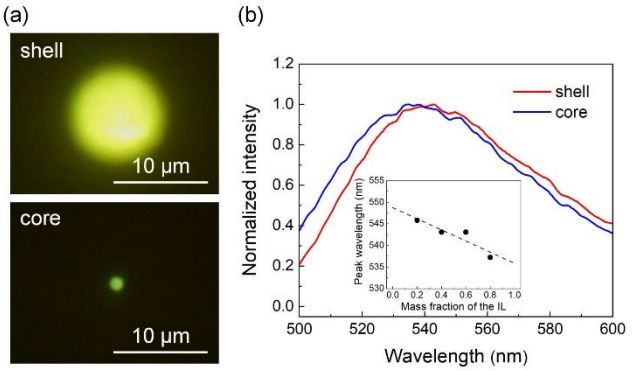

Fig. 4 Fluorescence (a) images and (b) spectra of the shell and the core.

We estimated the IL concentration on the basis of the fluorescence spectra of IL/water mixtures with different concentrations. The inset in Fig. 4b shows the peak wavelength against the mass fraction of the IL. Based on this calibration curve, the mass fraction of the shell was estimated to be 0.45, which matches well with the result from Raman spectroscopy. On the other hand, the core was calculated to have a mass fraction of almost 1.0. Due to the high IL concentration, the core is highly hydrophobic and has strong electrostatic interactions, due to which the core is stable for a long time.

Let us discuss the formation mechanism of the core-shell droplet described above. The solution used exhibits LCST-type phase separation, so that the solution temperature is crucial to consider the mechanism. The incident 1064-nm laser light is absorbed by the solution, and the temperature is elevated around the focal spot. It has been reported that the local temperature elevation when using optical tweezers can be calculated as a function of the absorption coefficient (α_{abs}), the thermal conductivity (k), and the input laser power (P).[31] The elevation (ΔT) is expressed by the following equation:

$$\Delta T = 0.75\frac{\alpha_{abs}}{k}P \quad (2).$$

The molar fraction of the IL is approximately 0.004 in the initial solution. Due to the low IL concentration, we assumed the initial solution to be just water and calculated the local temperature elevation using 14.5 m^{-1} for α_{abs}, 0.59 W/m·K for k, and 0.63 W for P. The elevation was estimated to be 12 K. The temperature around the focus is expected to be 48°C, which is much closer to the phase separation temperature.

The IL plays a role in enhancing the temperature elevation. We measured the absorption coefficient of the IL at 1064 nm using the reported method.[31] The α_{abs} of the IL was estimated to be 5.0 m^{-1}, about one third of the value of water. The thermal conductivity of the IL was calculated to be 0.19 W/m·K, which is based on the equation proposed by Fröba et al.[32,33] The value of α_{abs}/k of the IL is 1.07 times higher than that of water. Thus, the increase in IL concentration leads to higher temperature elevation during laser irradiation.

Due to one of the chemical properties of the IL, a droplet has a concentration distribution under laser irradiation.[28] The number of water molecules per ion pair in the IL phase decreases as the temperature rises. That is, the higher temperature generates condensates with greater IL concentration in phase separation. The incident laser has a Gaussian intensity profile, so that the solution temperature has a similar spatial distribution. Thus, the IL concentration should become high toward the center of the focal spot.

Figure 5 shows a schematic illustration of the possible dynamics of the formation of the core-shell droplet. In the early stage of irradiation, the solution temperature reaches around 49°C only at the focal spot (Fig. 5a), where the phase separation is induced. Resultant condensates gather in U_{opt} and develop into a small single droplet. The IL concentration becomes high toward the center of the droplet due to the temperature distribution (Fig. 5b). Such a droplet causes the temperature distribution to become higher and wider (Fig. 5c). The resultant higher temperature makes the droplet denser. Condensation accompanies the increase in α_{pol}, which deepens U_{opt}. In addition, further phase separation occurs at the outside of the

droplet due to the wider temperature distribution, leading to its growth (Fig. 5d). In this way, condensation and the growth of the droplet, deepening of U_{opt}, and a further temperature rise are repeated, like a positive feedback loop. As a result, the optical tweezers form a core-shell droplet whose core is stabilized in a deep U_{opt}.

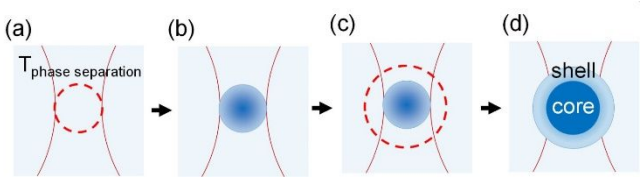

Fig. 5 Schematic illustration of the possible dynamics of a core-shell structure under focused laser irradiation.

A core-shell droplet is usually prepared with the use of two immiscible liquids, such as oil and water.[34] In such a case, the structure of the droplet will be determined by the physical and chemical properties of constituent liquids. In this study, the spatial difference in the optically and thermally formed potentials has a critical role to play in determining the droplet structure. These potentials can be modified by scanning a laser beam or using topological light waves such as optical vortices. The current approach may offer a new opportunity to fabricate not only a core-shell structure but also unique hetero-structures for various thermo-responsive materials. In addition, the mixture with photocurable resins may enable one to fix these unique structures permanently, which are possibly applicable to the research in fabrication, photonics, and analysis on the microscale.

This work was financially supported by JSPS KAKENHI grant numbers JP20H02550 JP20K05242 and by JST, CREST grant number JPMJCR1903. Also, the authors are grateful for financial support from the CANON Foundation.

Conflicts of interest

There are no conflicts to declare.

Notes and references

1 D. Erdemir, A. Y. Lee and A. S. Myerson, *Acc. Chem. Res.*, 2009, **42**, 621–629.
2 T. Okutsu, *J. Photochem. Photobiol. C Photochem. Rev.*, 2007, **8**, 143–155.
3 S. Boeynaems, S. Alberti, N. L. Fawzi, T. Mittag, M. Polymenidou, F. Rousseau, J. Schymkowitz, J. Shorter, B. Wolozin, L. Van Den Bosch, P. Tompa and M. Fuxreiter, *Trends Cell Biol.*, 2018, **28**, 420–435.
4 Y.-P. Chiu, Y.-C. Sun, D.-C. Qiu, Y.-H. Lin, Y.-Q. Chen, J.-C. Kuo and J. Huang, *Nat. Commun.*, 2020, **11**, 1229.
5 H. Cinar, Z. Fetahaj, S. Cinar, R. M. Vernon, H. S. Chan and R. H. A. Winter, *Chem. – A Eur. J.*, 2019, **25**, 13049–13069.
6 Q. Chen, P. G. Vekilov, R. L. Nagel and R. E. Hirsch, *Biophys. J.*, 2004, **86**, 1702–1712.
7 V. G. Taratuta, A. Holschbach, G. M. Thurston, D. Blankschtein and G. B. Benedek, *J. Phys. Chem.*, 1990, **94**, 2140–2144.
8 A. Abrishamkar, S. Suárez–García, S. Sevim, A. Sorrenti, R. Pons, S.-X. Liu, S. Decurtins, G. Aromí, D. Aguilà, S. Pané, A. J. deMello, A. Rotaru, D. Ruiz–Molina and J. Puigmartí-Luis, *Appl. Mater. Today*, 2020, **20**, 100632.
9 N. Calvo Galve, A. Abrishamkar, A. Sorrenti, L. Di Rienzo, M. Satta, M. D'Abramo, E. Coronado, A. J. de Mello, G. Mínguez Espallargas and J. Puigmartí-Luis, *Angew. Chemie Int. Ed.*, 2021, **60**, 15920–15927.
10 A. Sorrenti, L. Jones, S. Sevim, X. Cao, A. J. deMello, C. Martí-Gastaldo and J. Puigmartí-Luis, *J. Am. Chem. Soc.*, 2020, **142**, 9372–9381.
11 A. Ashkin, *Proc. Natl. Acad. Sci.*, 1997, **94**, 4853–4860.
12 Y. Harada and T. Asakura, *Opt. Commun.*, 1996, **124**, 529–541.
13 K. Yuyama, T. Sugiyama and H. Masuhara, *J. Phys. Chem. Lett.*, 2013, **4**, 2436–2440.
14 F. Walton and K. Wynne, *Soft Matter*, 2019, **15**, 8279–8289.
15 Z. Liao and K. Wynne, *J. Am. Chem. Soc.*, 2022, **144**, 6727–6733.
16 O. Y. Gowayed, T. Moosa, A. M. Moratos, T. Hua, S. Arnold and B. A. Garetz, *J. Phys. Chem. B*, 2021, **125**, 7828–7839.
17 F. Walton and K. Wynne, *Nat. Chem.*, 2018, **10**, 506–510.
18 T. Sugiyama, T. Adachi and H. Masuhara, *Chem. Lett.*, 2007, **36**, 1480–1481.
19 T. Sugiyama, K. Yuyama and H. Masuhara, *Acc. Chem. Res.*, 2012, **45**, 1946–1954.
20 H. Niinomi, T. Sugiyama, K. Miyamoto and T. Omatsu, *Cryst. Growth Des.*, 2018, **18**, 734–741.
21 T.-W. Shih, C.-L. Hsu, L.-Y. Chen, Y.-C. Huang, C.-J. Chen, Y. Inoue and T. Sugiyama, *Cryst. Growth Des.*, 2021, **21**, 6913–6923.
22 A. J. Alexander and P. J. Camp, *Cryst. Growth Des.*, 2009, **9**, 958–963.
23 J. Hofkens, J. Hotta, K. Sasaki, H. Masuhara, T. Taniguchi and T. Miyashita, *J. Am. Chem. Soc.*, 1997, **119**, 2741–2742.
24 M. Matsumoto, T.-A. Asoh, T. Shoji and Y. Tsuboi, *Langmuir*, 2021, **37**, 2874–2883.
25 N. Kitamura, K. Konno and S. Ishizaka, *Bull. Chem. Soc. Jpn.*, 2017, **90**, 404–410.
26 K. Ushiro, T. Shoji, M. Matsumoto, T.-A. Asoh, H. Horibe, Y. Katsumoto and Y. Tsuboi, *J. Phys. Chem. B*, 2020, **124**, 8454–8463.
27 S.-A. Mukai, N. Magome, H. Kitahata and K. Yoshikawa, *Appl. Phys. Lett.*, 2003, **83**, 2557–2559.
28 Y. Kohno, H. Arai, S. Saita and H. Ohno, *Aust. J. Chem.*, 2011, **64**, 1560–1567.
29 H. Kang, D. E. Suich, J. F. Davies, A. D. Wilson, J. J. Urban and R. Kostecki, *Commun. Chem.*, 2019, **2**, 51.
30 R. Karmakar and A. Samanta, *J. Phys. Chem. A*, 2002, **106**, 4447–4452.
31 S. Ito, T. Sugiyama, N. Toitani, G. Katayama and H. Miyasaka, *J. Phys. Chem. B*, 2007, **111**, 2365–2371.
32 A. Z. Hezave, S. Raeissi and M. Lashkarbolooki, *Ind. Eng. Chem. Res.*, 2012, **51**, 9886–9893.
33 A. P. Fröba, M. H. Rausch, K. Krzeminski, D. Assenbaum, P. Wasserscheid and A. Leipertz, *Int. J. Thermophys.*, 2010, **31**, 2059–2077.
34 P.-W. Ren, X.-J. Ju, R. Xie and L.-Y. Chu, *J. Colloid Interface Sci.*, 2010, **343**, 392–395.